PNAS
www.pnas.org

Supplementary Information for

Metal-insulator-transition engineering by modulation tilt-control in perovskite nickelates for room temperature optical switching

Zhaoliang Liao[a,1,2], Nicolas Gauquelin[b,1], Robert J. Green[c,d,1], Knut Müller-Caspary[b], Ivan Lobato[b], Lin Li[a], Sandra Van Aert[b], Johan Verbeeck[b], Mark Huijben[a], Mathieu N. Grisolia[e], Victor Rouco[e], Ralph El Hage[e], Javier E. Villegas[e], Alain Mercy[f], Manuel Bibes[e], Philippe Ghosez[f], George A. Sawatzky[c], Guus Rijnders[a], Gertjan Koster[a,2]

This PDF file includes:

Supplementary text
Figs. S1 to S8
References for SI reference citations

www.pnas.org/cgi/doi/10.1073/pnas.1807457115

1. Growth of the samples

The atomic flat $NdGaO_3$ (110) (NGO) substrates were treated by the etching of modified HF buffer solution and annealing at 1050 ^oC for 4 hour (1). All the materials of $SmNiO_3$ (SNO), $NdNiO_3$ (NNO), $LaNiO_3$ (LNO), $LaFeO_3$ (LFO) and $LaCrO_3$ (LCO) mentioned in the main text were deposited using pulsed laser deposition (PLD) technique at a laser fluence of 2 J/cm^2. During the growth, the temperature was maintained at 600 ^oC and oxygen pressure was 0.3 mbar. *In-situ* reflection high-energy electron diffraction (RHEED) was used to monitor the growth and confirmed a layer by layer growth fashion. After the growth, the samples were cooled down at 200 mbar at a cooling rate of 25 ^oC/min. For $(LFO_1/SNO_n)_m$ and $(LCO_1/SNO_n)_m$ superlattice growth, four unit cells (uc) of LFO and LCO layers were first deposited on NGO respectively and subsequent the superlattices were grown. For superlattices growth, it started from SNO layers. Since the LNO films with thickness more than about 3 unit cell (uc) are metallic, the $(LNO_1/SNO_n)_m$ superlattices were directly grown on NGO substrates. The surface morphologies of the films were characterized by atomic force microscopy (AFM). Figure S1A and S1B show respectively the AFM images of $(LFO_1/SNO_4)_{10}$ and $(LFO_1/SNO_{10})_4$ superlattices grown on NGO (110) substrates which confirm atomic flat surfaces with clearly visible terraces.

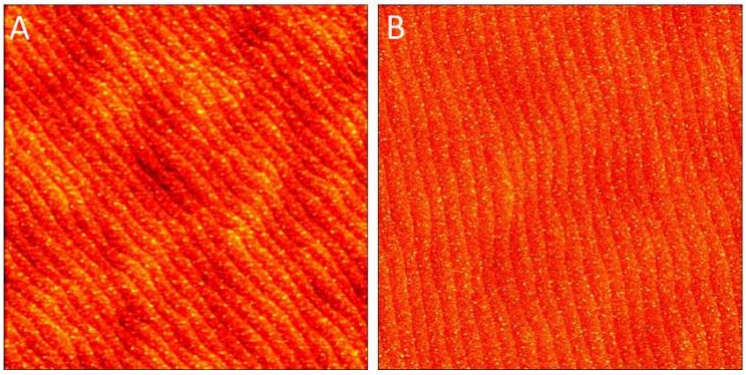

Figure S1: Surface morphology of (A) $(LFO_1/SNO_4)_{10}$ and (B) $(LFO_1/SNO_{10})_4$ superlattices by AFM. The size of the imaged area is 10x10 µm^2.

2. Structure characterization of nickelate superlattices

The lattice structures of the nickelate superlattices were characterized by x-ray diffraction (XRD) using PANalytical-X'Pert materials research diffractometer (MRD) at high resolution mode. Figure S2 presents the x-ray diffraction θ-2θ scan of LFO_1-SNO_4 superlattice which shows satellite peaks originating from the superlattice structure. The superlattice peaks (SL0, SL+1, SL-1) reveal a superlattice period of 1.92 nm, fully consistent with the designed period controlled during growth by RHEED intensity oscillation. The presence of Pendellösung fringes further confirm the smoothness of the surface and the high quality ordering of the superlattice. The high structural quality of a bare 30 uc SNO film (SNO_{30}) is also indicated by XRD in Fig. S2A.

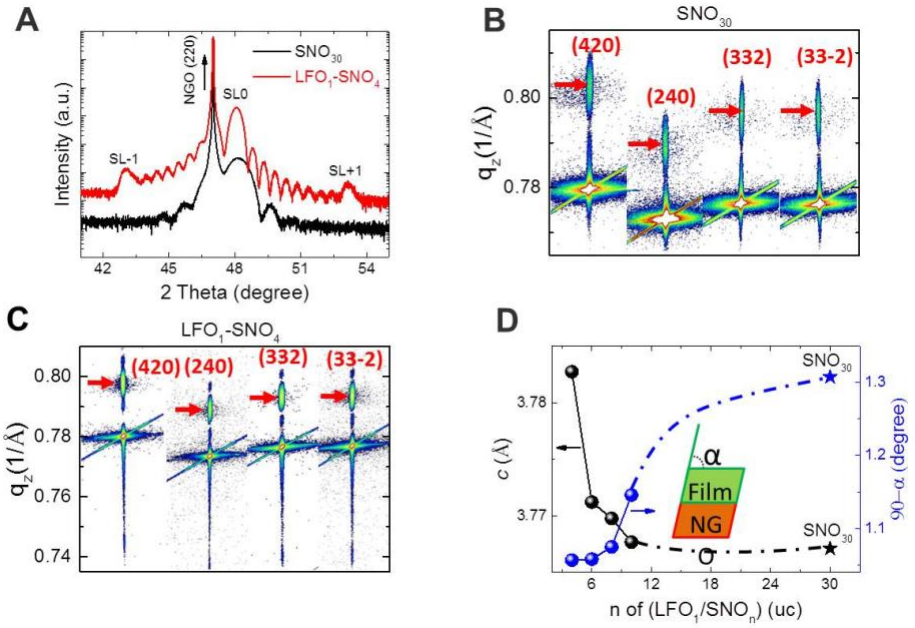

Figure S2: (A) X-ray diffraction θ-2θ scan of SNO_{30} film and LFO_1-SNO_4 superlattice. (B) Reciprocal space mapping of the (420), (240), (332) and (33-2) reflections of (B) SNO_{30} film and (C) LFO_1-SNO_4 superlattice. The peaks are noted in orthorhombic indices. (D) Lattice parameters of LFO_1-SNO_n superlattice (sphere dots) as a function of SNO layer thickness and SNO_{30} film (star symbol).

The lattice structures of LFO_1-SNO_n superlattices and SNO films have been characterized by high resolution x-ray reciprocal space mapping (RSM). Figure S2B and S2C show respectively the RSMs of the (420), (240), (332) and (33-2) reflections of SNO_{30} film and LFO_1-SNO_4 superlattice, which both indicate orthorhombic structures. Note that upon conversion of this (110)-oriented orthorhombic structure into a pseudocubic unit cell, a monoclinic tilt angle α appears. The out-of-plane lattice parameter *c* and monoclinic tilt angle α of SLs in pseudocubic unit cell exhibit a gradual change with increasing SNO thickness n. As shown in Fig. S2D, *c* gradually decays to that of bulk SNO film value and $\frac{\pi}{2} - \alpha$ gradually increases to that of bulk SNO film, suggesting reduced structural distortion in SLs when the SNO layer is very thin and the impact of the LFO is strong.

3. Chemical contrast across the nickelate superlattices

All scanning transmission electron microscopy (STEM) images were processed as follow: 20 images were acquired with a beam current of 40 pA and a fast acquisition time of 0.1 µs/pixel. Each image resolution was 4096*4096 pixels. These images were then aligned and drift corrected as described in Ref. 32. From the corrected images, the StatSTEM software was used to measure the position coordinates of each atomic column using statistical parameter estimation theory (2). All subsequent parameters (tilt angles, intensity profiles, c lattice parameter, strain, etc.) were extracted using the ImageEval software (3).

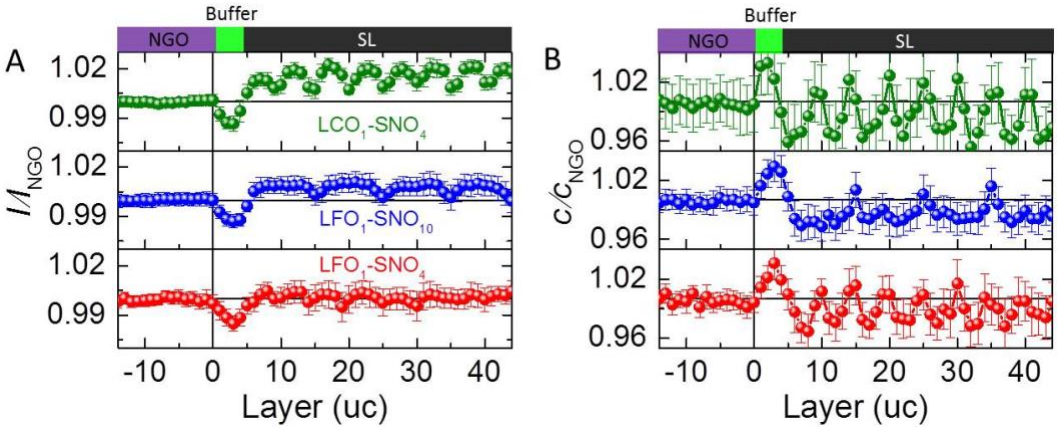

Figure S3: (A) Normalized HAADF-STEM intensity (I/I_{NGO}) profiles and (B) normalized lattice constant (c/c_{NGO}) profiles for three superlattices: $(LFO_1/SNO_4)_{10}$ (red), $(LFO_1/SNO_{10})_4$ (blue) and $(LCO_1/LFO_4)_{10}$ (green).

The limited contrast between LFO and SNO in high angle annular dark field (HAADF) STEM images is due to the high similarity of their atomic number for Sm (62), Nd (60) and La (57) on the A-sites, as well as Ni (28) and Fe (26) on the B-sites. The intensity of a STEM image depends on the atomic number (Z) and a larger Z will give rise to a higher intensity. Therefore, there should be still intensity contrast although it is small and may be too small to be resolved by eye directly from a HAADF-STEM image. Figure S3A plots the STEM intensity profiles for three different samples of $(LFO_1/SNO_4)_{10}$, $(LFO_1/SNO_{10})_4$ and $(LCO_1/LFO_4)_{10}$ superlattices. The intensities are calculated from their HAADF images with zone axis along [1-10] and the intensities are normalized to the intensity of the NGO substrates. The intensity contrast indeed is very low. For example, the intensity of LFO from buffered region is only about 2% lower than that of the NGO substrate. However, the contrast can be still resolved in intensity-profile where the valley positions indicate the LFO layers and peak positions suggest the center of the SNO layers. A periodic modulation of the intensity can be observed for all three $(LFO_1/SNO_4)_{10}$, $(LFO_1/SNO_{10})_4$ and $(LCO_1/LFO_4)_{10}$ superlattices, confirming the superlattice structures.

The chemical contrast can also be reflected from the profile of out-of-plane lattice parameter (*c*). Since the LFO or LCO will have larger lattice constant than NGO or SNO, peak positions can then suggest us the location of the LFO or LCO layers. As shown in Fig. S3B, a larger *c* lattice parameter is observed in the buffer LFO or LCO regions. Within the superlattice area, a periodic modulation of *c* axis length is observed with larger (smaller) values in LFO (SNO) layers. Due to interfacial octahedral coupling effect, there are mutual geometry constraint of octahedral tilt of SNO and LFO. The LFO will reduce the tilt of SNO at the LFO/SNO interfaces, but the SNO reciprocally forces the tilt of LFO to be larger. This effect will make the tilts of LFO within the superlattice region larger than that of the first 4 uc LFO buffer. As a result, the *c* of LFO within superlattice is also smaller than the LFO buffer. In contrast, the SNO will have larger *c* near LFO/SNO interfaces and smaller *c* in the central part of SNO (see red and blue

curves in Fig. S3B). Similar scenario occurs for $(LCO_1/SNO_4)_{10}$ superlattice (see green curve in Fig. S3B).

4. Electron energy loss spectroscopy (EELS) maps

The chemical contrast across the nickelate superlattice has also been characterized by electron energy loss spectroscopy (EELS) mapping. Figure S4 shows the EELS mapping of $(LFO_1/SNO_4)_{10}$ superlattice. The first panel is the simultaneously acquired annular dark field (ADF) image, indicating consistent atomic ordering across the superlattice. The good quality of the superlattice and atomic sharpness of the interfaces within the superlattice is suggested from the atomic resolved EELS mapping of Sm $M_{4,5}$, La $M_{4,5}$, Fe $L_{2,3}$, Ni $L_{2,3}$. EELS mapping shows a periodic stacking of 4 uc SNO and 1 uc LFO. There is slight diffusion of La at the LFO/SNO interface. The LFO layer always consists of one FeO_2 layer followed by a LaO layer. This indicates that the layer stacking at the SNO_4-LFO_1-SNO_4 interfaces has the following sequence: NiO_2-SmO-FeO_2-LaO-NiO_2-SmO.

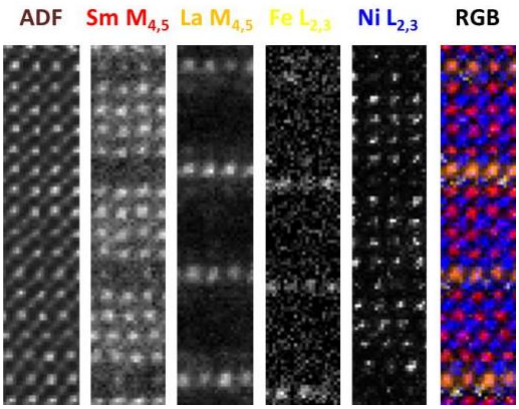

Figure S4: Atomically resolved EELS mapping of Sm $M_{4,5}$, La $M_{4,5}$, Fe $L_{2,3}$, Ni $L_{2,3}$ at the $(LFO_1/SNO_4)_{10}$ superlattices. The first panel is the simultaneously acquired annular dark field (ADF) image. For RGB composite at last panel, the following color was used: red: Sm; orange: La; yellow: Fe; Blue: Ni.

5. Estimation of lattice parameters profiles

Using statistical parameter estimation theory, atomic column positions (X,Y) in scanning transmission electron microscopy images can be precisely determined (2, 4-6) and thus detailed lattice structure parameters can be quantified statistically. To quantify the layer-position dependent octahedral tilt distortion, inversed annular bright field STEM (ABF-STEM) images which enable us to resolve the oxygen sites are used while for the A-site displacement quantification, HAADF images which have better contrast for heavier elements are chosen. Figure S5A shows a 2D mapping of the the angle Φ for a $(LFO_1/SNO_{10})_4$ superlattice. The definition of the angle is shown in the inset of Fig. S5A. The angle Φ is the angle between three successive A-sites in the same row in (1-10) plane. To reflect the rumpling feature of A-sites we define Φ_{A_2}as $\angle A_1A_2A_3 - \pi$ while

$\Phi_{A_3} = \pi - \angle A_2 A_3 A_4$, thus we will have an alternated sign of Φ (…+-+-+-…). Figure S5A shows a 2D mapping of the signed Φ of $(LFO_1/SNO_{10})_4$ sample from a HAADF image. The mapping of Φ is overlaid on the HAADF image. A checkboard pattern can be seen in the signed Φ mapping due to the alternated sign of the Φ. We can also use the unsigned Φ by taking the absolute value of this angle and obtain a mapping of unsigned Φ as shown in Fig. S5B. Figure S5C also shows a 2D mapping of unsigned Φ for $(LFO_1/SNO_4)_{10}$ superlattice. With these 2D maps, we can average the unsigned Φ in the same layer and then obtain the layer-position dependent mean Φ together with its standard deviation across the samples presented in Fig 3D of the main text.

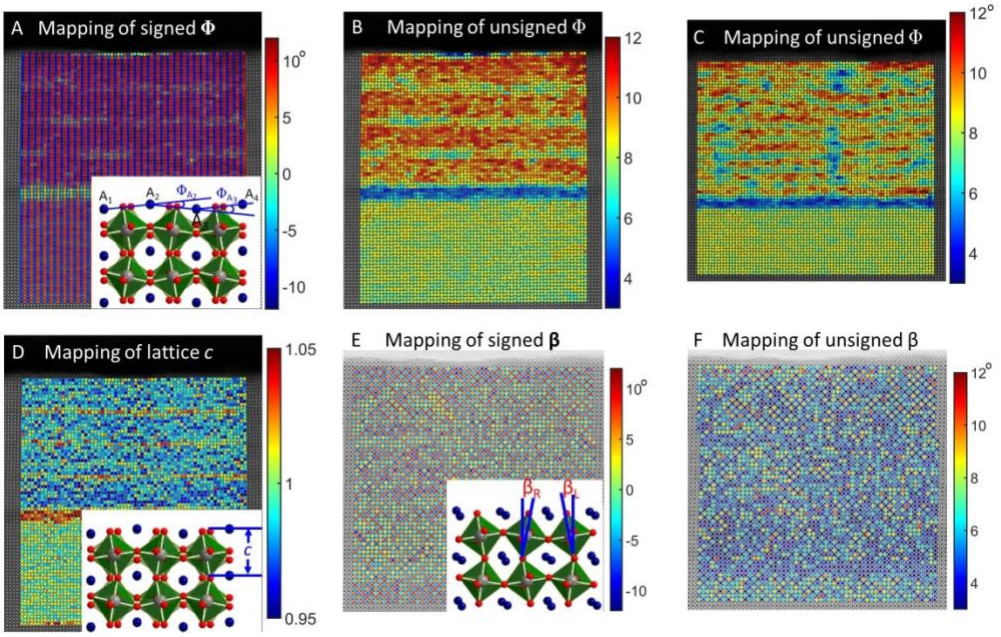

Figure S5: 2D mapping of (A) signed and (B) unsigned anti-polar A-site motion (Φ) in $(LFO_1/SNO_{10})_4$ superlattice. (C) 2D mapping of unsigned Φ angle in $(LFO_1/SNO_4)_{10}$ superlattice. (D) 2D mapping of out-of-plane lattice parameter *c* in $(LFO_1/SNO_{10})_4$ superlattice. The *c* is normalized to the lattice *c* of NGO substrate. 2D mapping of (E) signed **β** and (F) unsigned β angle in $(LFO_1/SNO_4)_{10}$ superlattice. For all mappings, each color pixel represents a local angle at a specific local A-site (A)-(C), local lattice parameter *c* at a specific single unit cell (D) or local octahedra tilt angle β at a local specific BO_6 octahedron (E)-(F). The 2D mappings are overlaid on HAADF images or ABF images from which corresponding lattice structure parameters are calculated

The out-of-plane lattice parameter (*c*) profile is calculated from the 2D mapping of *c*. The definition of the *c*-axis is shown in inset of Fig. S5D, which is the lattice spacing between two nearest neighboring AO planes. An example of the 2D mapping of *c* of $(LFO_1/SNO_{10})_4$ superlattice is shown in Fig. S5D. Here, the *c* is normalized to the substrate NGO *c* value. Similar to the calculation of Φ-profile, we can also average the *c* in each layer and then obtain the layer position dependent mean *c* together with its standard deviation presented in Fig. 3F of the main text.

While the profile of octahedral tilt angle β around the [001] axes is determined from the 2D mapping of β from ABF images. Figure S5E shows a 2D mapping of the signed β angle of $(LFO_1/SNO_4)_{10}$ superlattice. The definition of β is shown in inset of Fig. S5E. The β of left tilted octahedron is defined as negative value and right tilted octahedron as positive value. Taking the absolute value of the β, the signed β mapping is then converted into unsigned β mapping as shown in Fig. S5F. By averaging the unsigned β in the same layer, the layer-position dependent mean β together with its standard deviation across the samples presented in Fig 3E of the main text is obtained.

6. Phase diagram of $(LaFeO_3)_1$-$(SmNiO_3)_n$ superlattices

The thickness (n) of SNO within LFO_1-SNO_n SLs effectively controls the transition temperatures. By plotting the MIT temperature (T_{MIT}) and Néel temperature (T_N) as a function of SNO thickness (n), a phase diagram is constructed and shown in Fig. S6. The T_{MIT} monotonically increases the increasing n. The phase diagram is similar to bulk phase diagram where the tolerance factor is used as control parameter. For superlattices with a relatively low T_{MIT} (< ~200 K), their T_N is coincident with T_{MIT}. For superlattices with T_{MIT} larger than ~200 K, the T_N and T_{MIT} are decoupled and show an increase in temperature difference with increasing T_{MIT}.

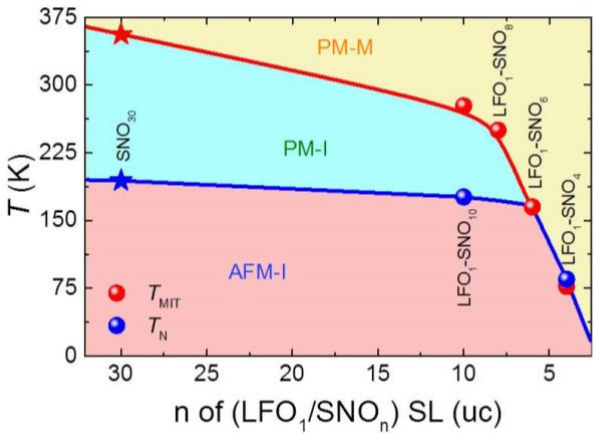

Figure S6: Controlled transition temperature (T_{MIT}, T_N) by changing the thickness of the SNO layers in LFO_1-SNO_n superlattices.

7. Metal-insulator transition in $NdNiO_3$-$SmNiO_3$ superlattices

In order to realize room temperature oxide electronics for practical application, a proper tilt control layer is explored to induce first order room temperature metal-insulator transition. Several tilt control layers have been tried, such as $LaFeO_3$, $LaCrO_3$, $LaNiO_3$, and $NdNiO_3$. Among those tilt control layers, the $NdNiO_3$ is found to be an ideal candidate to induce sharp first order room temperature metal-insulator transition. The tilting of octahedra can be controlled by constructing $((NdNiO_3)_m/(SmNiO_3)_n)_N$ superlattices on NGO (110) substrates which is denoted by NNO_m-SNO_n for simplify. The thickness of the superlattice is maintained to be ~ 30 uc. Since the tilt of NNO is smaller, their combination will lead to an octahedral tilt in between NNO and SNO, thus tuning the T_{MIT} in between that of NNO and SNO depending on the ratio of n/m. As

shown in Fig. S7, increasing the n/m from 2/2 to 3/1 gradually increases T_{MIT}. The first order metal insulator transition is obtained for NNO_2-SNO_2 and NNO_1-SNO_2 superlattices while it is more cross-over like in NNO_1-SNO_3 superlattice. Interestingly, near room temperature sharp metal-insulator (T_{MIT} = 293 K) is obtained for NNO_1-SNO_2 superlattice, providing great opportunity for fabricating room temperature electronics device.

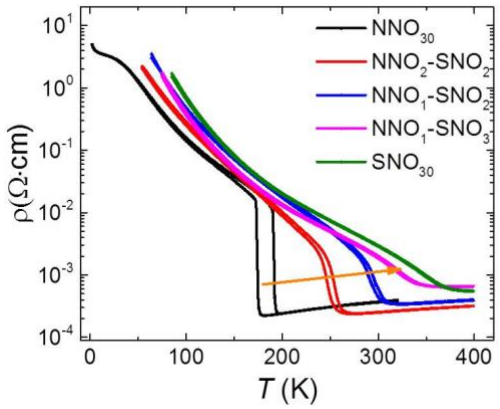

Figure S7: Metal-insulator transition in NNO_m-SNO_n superlattices. The orange arrow indicates the tendency of the change of T_{MIT} with increasing n/m ratio.

8. Optical experiments in nickelate superlattices

Transport measurements under illumination were performed in a MONTANA cryostation with uncoated windows presenting 90% transmittance in the visible range. Two different configurations were used for characterizing the thermal response of the samples. In Setup-1, the layer was thermally connected to the cold finger of the cryostat. To do so we added thermal grease to the edges of the sample in such a way that the $NdGaO_3$ substrate was thermally connected to the sample holder. In Setup-2, an insulating layer was added between the sample and the sample holder such that there was no thermal contact between the layer and the cold finger of the cryostat. The sheet resistance was determined by biasing with a current of 10 µA.

Figure S8 presents the results of these experiments on two superlattices: SNO_{10}-LFO_1 (panels a and b) and SNO_3-NNO_2 (panels c and d) with Setup-1 (panels a and c) and Setup-2 (panels b and d). In isothermal illumination (Setup-1, panels a and c), a very small resistance change is observed, showing a peak in temperature reminiscent of the metal-insulator transition. Note that for the SNO_3-NNO_2 sample, this peak is superimposed with a negative background reflecting a slight change of the overall sample resistance between the two consecutive temperature sweeps. In non-isothermal illumination (Setup-2, panels b and d), the relative resistance change is much stronger, up to a factor 2-3. Again, for both samples, its temperature dependence shows a peak related to the metal-insulator transition (for the SNO_{10}-LFO_1 sample this peak is superimposed with a decrease, reflecting the thermally activated transport behavior in the insulating state). The difference in the response between both setups strongly suggests that light illumination promotes sample heating, however with a specific wavelength dependence

as we discuss in the manuscript.

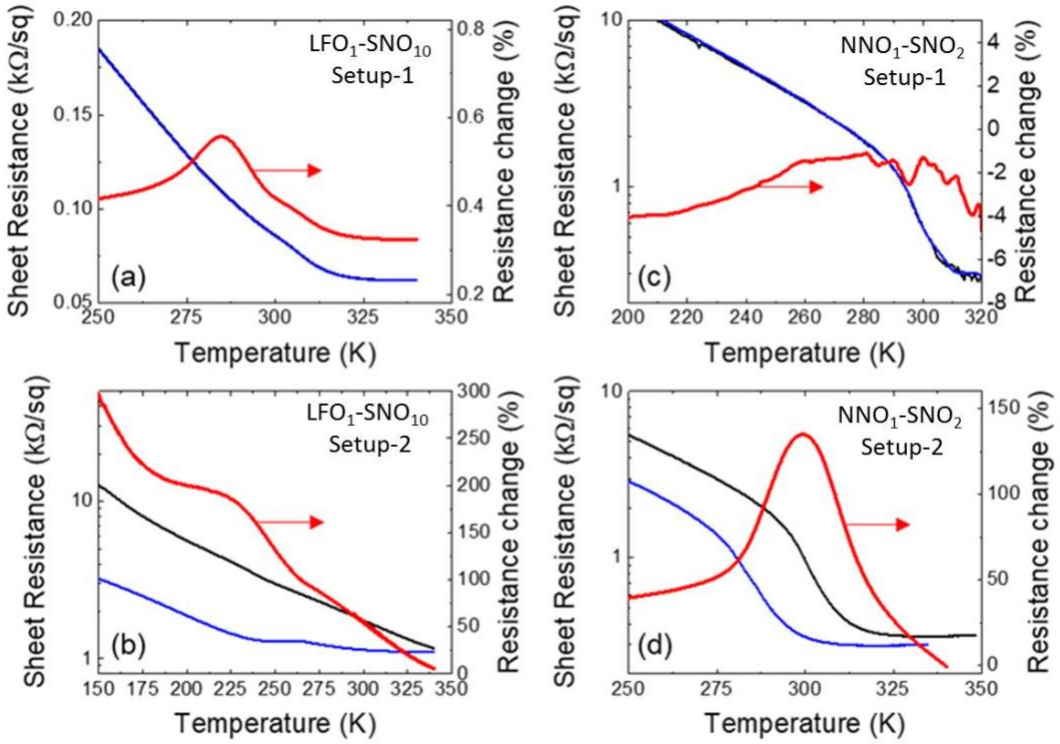

Figure S8: Temperature dependence of the resistance for LFO_1-SNO_{10} and NNO_1-SNO_2 superlattices in two experimental configurations (Setup-1 and Setup-2).

References

[1] V. Leca, D. H. A. Blank, G. Rijnders, Termination control of $NdGaO_3$ crystal surfaces by selective chemical etchingarXiv:1202.2256.

[2] A. De Backer, K.H.W. van den Bos, W. Van den Broek, J. Sijbers and S. Van Aert, StatSTEM: an efficient approach for accurate and precise model-based quantification of atomic resolution electron microscopy images, *Ultramicroscopy* **171**, 104 (2016).

[3] K. Müller-Caspary, T. Mehrtens, M. Schowalter, T. Grieb, A. Rosenauer, F. F.Krause, C. Mahr, and P. Potapov, ImageEval. A software for the processing, evaluation and acquisition of (S)TEM images, *European Microscopy Congress* 2016: Proceedings. 481–482

[4] A.J. den Dekker, S. Van Aert, A. van den Bos and D. Van Dyck, Maximum likelihood estimation of structure parameters from high resolution electron microscopy images. Part I: A theoretical framework, *Ultramicroscopy* **104**, 83 (2005).

[5] S. Van Aert, A.J. den Dekker, A. van den Bos, D. Van Dyck and J.H. Chen, Maximum likelihood estimation of structure parameters from high resolution electron microscopy images. Part II: A practical example, *Ultramicroscopy* **104**, 107 (2005).

[6] N. Gauquelin, KHW. van den Bos, A. Béché, F.F. Krause, L. Lobato, S. Lazar, A. Rosenauer, S. Van Aert, J. Verbeeck, Determining oxygen relaxations at an interface: A comparative study between transmission electron microscopy techniques, *Ultramicroscopy* **181**, 178 (2017).